Garcia-Mulero, A.; Asiri, AM.; Albero-Sancho, J.; Primo Arnau, AM.; García Gómez, H. (2022). All-carbon microporous graphitic photocatalyst-promoted reduction of CO2 to CO in the absence of metals or dopant elements. Nanoscale. 14(32):11575-11582. https://doi.org/10.1039/d2nr02655d

An all-carbon microporous graphitic photocatalyst promotes CO_2 reduction to CO in the absence of metals or dopant elements.

Ana García-Mulero,[a] Abdullah M. Asiri,[b] Josep Albero,[a] Ana Primo[a] and Hermenegildo Garcia[a,b]

[a] Instituto Universitario de Tecnología Química, Consejo Superior de Investigaciones Científicas-Universitat Politecnica de Valencia, Universitat Politecnica de Valencia, 46022 Valencia

[b] Center of Excellence in Advanced Materials Research, King Abdullah University, Jeddah, Saudi Arabia

Abstract.

Microporous graphitic carbons (mp-C) derived from pyrolysis of α, β and γ–cyclodextrins exhibit upon irradiation with UV-Vis light photocatalytic activity in CO_2-saturated acetonitrile-water in the presence of triethanolamine, forming H_2 (19 $\mu mol \times h^{-1}$) and CO (23 $\mu mol \times h^{-1}$) accompanied by lesser proportions of CH_4 (4 $\mu mol \times h^{-1}$). The most efficient being the mp-C material derived from α-cyclodextrin (mp-C_α) and having a pore dimension of 0.68 nm. The process occurs, although with much lesser extent, under simulated sunlight or with UV-Vis irradiation in the absence of sacrificial agent, H_2O being the electron donor. The origin of CO has been proved by isotopic ^{13}C labelling experiments. Photocurrent measurements prove the occurrence

of charge separation and the increase in photocurrent intensity in the presence of CO2. Transient absorption spectroscopy detects the charge separate state decaying in the microsecond time scale and proves that a fraction of the photogenerated electrons are able to react with CO_2.

Introduction.

Photocatalysis is gaining interest as a long-term technology to produce from abundant feedstocks fuels and chemicals using directly sunlight.[1] Since the seminal discovery by Fujishima and Honda on the photoelectrocatalytic activity of TiO_2 under UV irradiation,[2,3] photocatalysis has been traditionally dominated by transition metal semiconductors.[3,4] However, for the sake of sustainability and considering the scarcity of resources, there is much current interest in moving from metal-containing catalysts to metal-free catalysts,[5-7] also in the area of photocatalysis.[8] The number of examples showing that metal-free materials can behave as photocatalysts, even for overall H_2O splitting, is increasing continuously. Compared to H_2 generation, photocatalytic CO_2 reduction is considerably more challenging due to the sluggish kinetics involved in the transfer of several electrons and protons.[9] An additional factor to be considered is CO_2 adsorption on the photocatalyst surface. For this reason the number of metal-free photocatalysts for CO_2 reduction is comparatively lower, there being a need to expand the number of materials under study, particularly those based predominantly on carbon.[10]

In this context, defective doped graphenes have shown activity for H_2 generation.[11] More recently, microporous graphitic carbons (mp-C) derived from cyclodextrins have also shown photocatalytic activity for hydrogen generation and oxygen evolution.[12] Theoretical calculations indicate that oxidation sites can be associated to the residual population of oxygen atoms in the microporous graphitic materials.[13] In addition, these calculations also indicate that confinement inside the micropores can facilitate bond cleavage in a kind of preactivation when the size of the molecules fit tight within the graphenic wall of the microporous carbon.[13] Photocatalytic hydrogen evolution activity increases upon N- or P-doping as consequence of band alignment, the resulting mp-(N)C and mp-(P)G powders being able to even promote overall H_2O splitting.

Going further in the study of the photocatalytic activity of this type of metal-free microporous graphitic carbons, it would be of interest to determine if these novel materials can also promote the photocatalytic CO_2 reduction, a reaction that is more challenging than hydrogen generation from water, due to the need of larger reduction potentials and the large range of products that can be formed. Herein it is reported that, in the absence of any metal, microporous graphitic carbons exhibit photocatalytic activity for the selective CO_2 reduction to CO in the presence of sacrificial electron donors and that this photocatalytic activity follows the trend observed for overall water splitting, the most efficient material being the one derived from the smallest α-cyclodextrin.

Results and discussion.

The mp-C materials (mp standing for microporous and C corresponding to graphitic carbon) under study were obtained by pyrolysis at 900 ºC under inert atmosphere of α–, β– and γ–cyclodextrins as previously reported. N- and P-doping was achieved by mixing homogeneously urea or H_3PO_4 to the cyclodextrin in the proportion indicated before the pyrolysis. The resulting samples were characterized by combustion elemental analysis. Analytical data of the samples under study are presented in Table 1. Importantly, mp-Cα is constituted almost exclusively by C (>99 %) and some residual H. In comparison, oxygen is present in about 9 and 13 wt% in mp-Cβ and mp-Cγ, respectively. This trend in the O content depending on the pore dimension of the resulting mp-C was already observed and suggest that oxygen functionalities are better accommodated in larger pores, while their content in mp-Cα is almost negligible. This oxygen content also increases upon doping, in which in addition to the dopant element the presence of a substantial percentage of oxygen (above 10 %) should also be noted. The extent of N- and P-doping was also determined by elemental analysis.

Specific surface area of microporous carbons was measured by isothermal CO_2 adsorption at 273 K. At this point it should be commented that in contrast to CO_2 mp-Cα does not adsorb N_2, a fact that was attributed to its pore size (0.64 nm) close to the N_2 kinetic diameter in comparison with the pore size of mp-Cα and mp-Cα that are 0.78 and 0.99 nm, respectively. A remarkable fact is the significantly much larger area of mp-(P)Cα. It is proposed that the weak acidity of H_3PO_4 used as P precursor is responsible for some

additional corrosion of the graphenic walls during the pyrolysis process, leading to a three-fold specific surface area increase.

Table 1. Analytical data of the different synthetized samples, surface area and band gap.

Material	%C	%H	%N	%other	Surface área (m^2/g)	Band gap (eV)	Valence band (eV)
mp-C_α	98,21	1	0	0	572	3,3	2.2
mp-C_β	89,17	1,166	0	0	597	3,0	2.5
mp-C_γ	86,95	0,605	0	0	630	2,8	2.9
mp-(P)C_α	87,38	1,078	0	1,94% P	1928	3,1	1.8
mp-(N)C_α	80,88	0,950	3,36	0	540	2	1.7

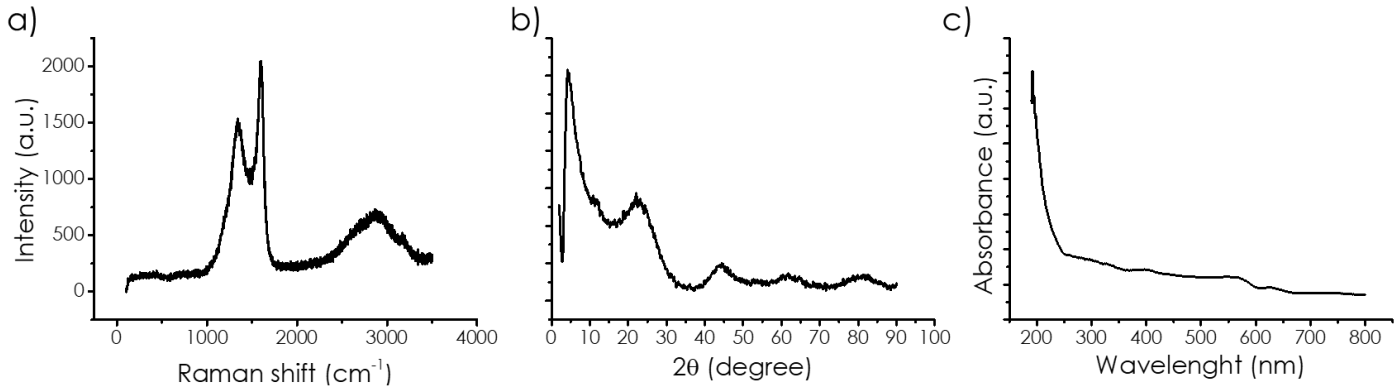

Figure 1. a) Raman spectra; b) XRD pattern and c) UV-Vis spectra of the sample mp-C_α.

Raman spectra of the mp-C samples were almost coincident. As an example Fig. 1 shows a representative example and Fig. S1 in the Supporting Information gathers the Raman spectra of the samples under study. Three signals corresponding to 2D (broad), G and D bands appearing at about 2700, 1590 and 1350 cm^{-1}, respectively, were recorded. These three signatures are characteristic of defective graphenes derived from oligo or polysaccharides. Doping was not reflected in any detectable change in Raman spectroscopy.

The high crystallinity of the mp-C is reflected in the XRD patterns of the powders. Fig. 1 also presents a selected example and the collection of XRD patterns are gathered in Fig. S2 in the Supporting Information. Broad peaks corresponding to the loose stacking of graphene sheets at about 26, 45 and 61 and 80 º corresponding to the 002, 004, 113 and 110???? Faces diffractions were recorded. In addition, a new diffraction peak at short angles that is attributable to the presence of the micropores is also recorded for mp-C.

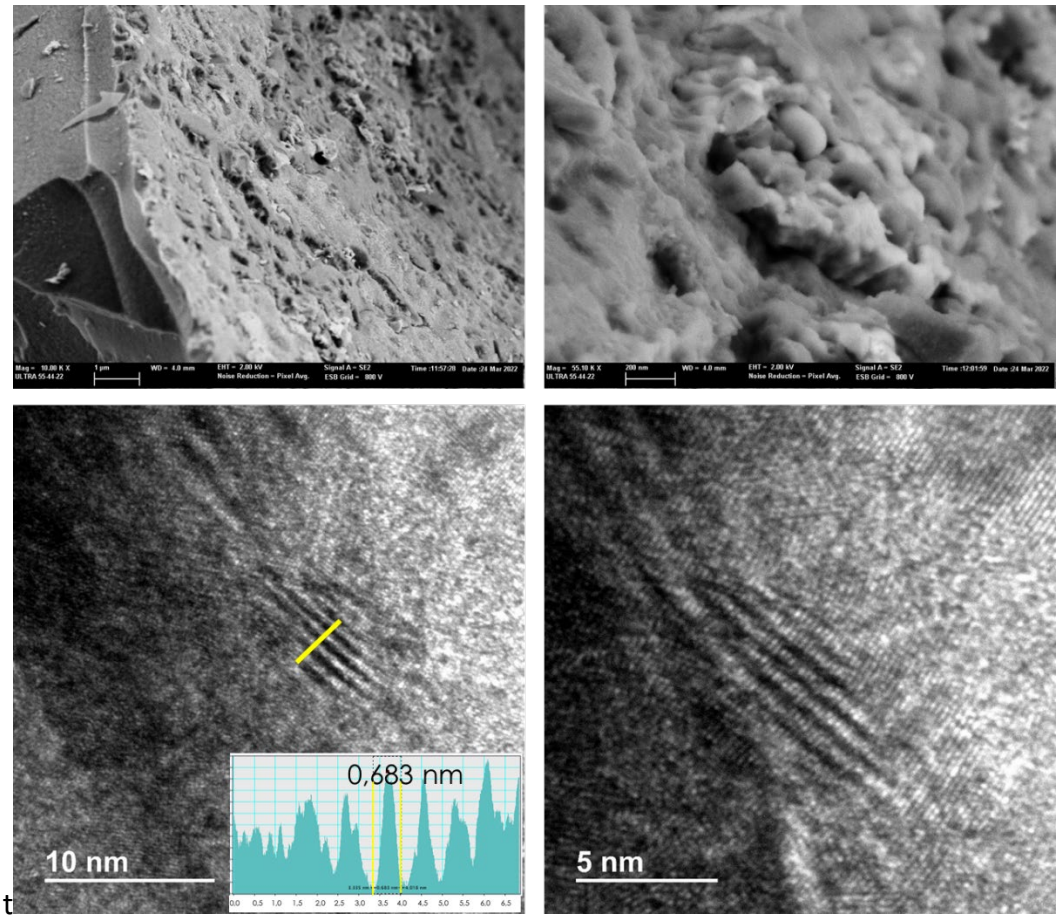

t

Figure 2. Field Emission Scanning Electron Microscope and Transmission Electron Microscope images of the mp-C$_\alpha$.

The morphology of the particles was determined by field-emission scanning electron microscopy (Fig. 2 and S3 in Supporting Information). It was observed that upon pyrolysis, the cyclodextrin powders form a thick crust carbon residue with smooth surface, due to the melt of cyclodextrin powder and the transformation into graphitic carbon. Inspection at a higher magnification of the crust reveals the presence of granules arranged forming tubular agglomerates most of them longer than one micron length and about 80 nm wide, aligned perpendicular to the surface. Transmission electron microscopy reveal the presence of

small particles of about 10-20 nm having microporous channels. Fig. 2 shows a selection of these TEM images. From the contrast between the walls and the voids, the pore size was estimated as 0.68, 0.86 and 0.97 nm for mp-C_α, mp-C_β and mp-C_γ, respectively. These values are in good accordance with data previously reported, showing that the dimensions of the cyclodextrin precursor determines the dimensions of the pores in the resulting graphitic carbon.

Diffuse-reflectance UV-Vis absorption spectra of the samples under study were also very similar with a continuous absorption all over the range of UV and visible wavelengths decreasing gradually in absorptivity towards longer wavelengths. Fig. 1 also includes a representative DR-UV-Vis spectra and the collection for all the samples is presented in Fig. S4 in supporting information. Some relative absorption maxima were measured at 280, 400, 550 and 620 nm, coincident for all the mp-C samples. N- and P-doping modifies the DR-UV-Vis spectra mostly in the UV region, by introducing a more intense absorption band with a tail extending to 350 and 300 nm for mp-(N)C_α and mp-(P)C_α, respectively, while no influence was observed at longer wavelengths. From the optical absorption spectroscopy the bandgap of the samples could be estimated using the Tauc plot. The optical bandgap for each mp-C sample is provided also in Table 1.

Photocatalytic activity.

Photocatalytic CO_2 reduction reactions using the mp-C samples as photocatalysts (15 mg) were carried out in mixture of acetonitrile (12 mL) and H_2O (4 mL) adding triethanolamine (TEOA) (4 mL) as sacrificial electron donor, using the output of a 300 W Xe

lamp. The course of the reaction was followed taking aliquots of the head space that were analyzed in a micro-GC. Experimental section provides additional details of the reactor, CO_2 pressure and analysis. The products observed under these conditions were H_2 and CO in similar amounts, accompanied by a lesser proportion of CH_4. No products in the liquid phase were detected at the end of the reaction by ^1H and ^{13}C NMR spectroscopy. Fig. 3 shows the temporal evolution of the three gases using mp-C_α as photocatalyst, while Fig. S5 in supporting presents a complete series of plots for each of the mp-C under study. The photocatalytic activity for H_2 or CO evolution follows the order mp-C_α>mp-C_β≈mp-C_γ. This order is similar to what has been observed for H_2 generation and it has been interpreted as reflecting the beneficial influence of confinement and small pore size commensurate with the substrate dimensions to enhance the photocatalytic activity.[12] No beneficial influence of doping on the photocatalytic CO_2 reduction to CO was observed and the performance of mp-C_α was also higher than those of mp-(N)C_α and mp-(P)C_α (see Fig. S5). In view of these results, one aspect that is remarkable is the higher efficiency of a material such as mp-C_α constituted in higher than 99 % by C element in the absence of any metal or even dopant element. In the state of the art is frequently assumed that doping in the optimal proportion should increase the photocatalytic activity of graphitic carbons, but this assumption does not seem applying in the present set of samples. It could be that the mp-C_α contains excessive dopant loadings. Apparent quantum yield of CO formation measured for mp-C_α at 380 nm was determined as 0.02 %.

Photocatalyst stability was checked by performing a set of consecutive uses with the same mp-C sample, whereby observing similar temporal evolution profiles for H_2, CO and

CH_4 in four consecutive uses (Fig. S6). Furthermore, TEM characterization of the mp-C sample after exhaustive use show that porosity and morphology of the sample was maintained in the process. These photocatalytic data and characterization support photocatalyst stability under irradiation conditions.

Under the same solvent mixture and conditions, but using solar simulated sunlight, mp-C was also active, although with lesser gas evolution. The results are presented in Fig. S7 in the supporting information. Notably, CH_4 (8 $\mu mol \times h^{-1}$) was the major product formed under these conditions, with a significantly lesser evolution of H_2 (1.3 $\mu mol \times h^{-1}$) and CO (2 $\mu mol \times h^{-1}$). This product dependence with the irradiation wavelength would indicate the existence of different sites in mp-C. It is proposed that CH_4 is the product formed when there is a strong CO adsorption as consequence of the deeper photocatalytic reduction. If this were the case, then, CO would be formed in those sites with less CO affinity, while CH_4 would be on those other with stronger CO adsorption. It seems that those sites with stronger CO affinity are responsive to longer wavelengths.

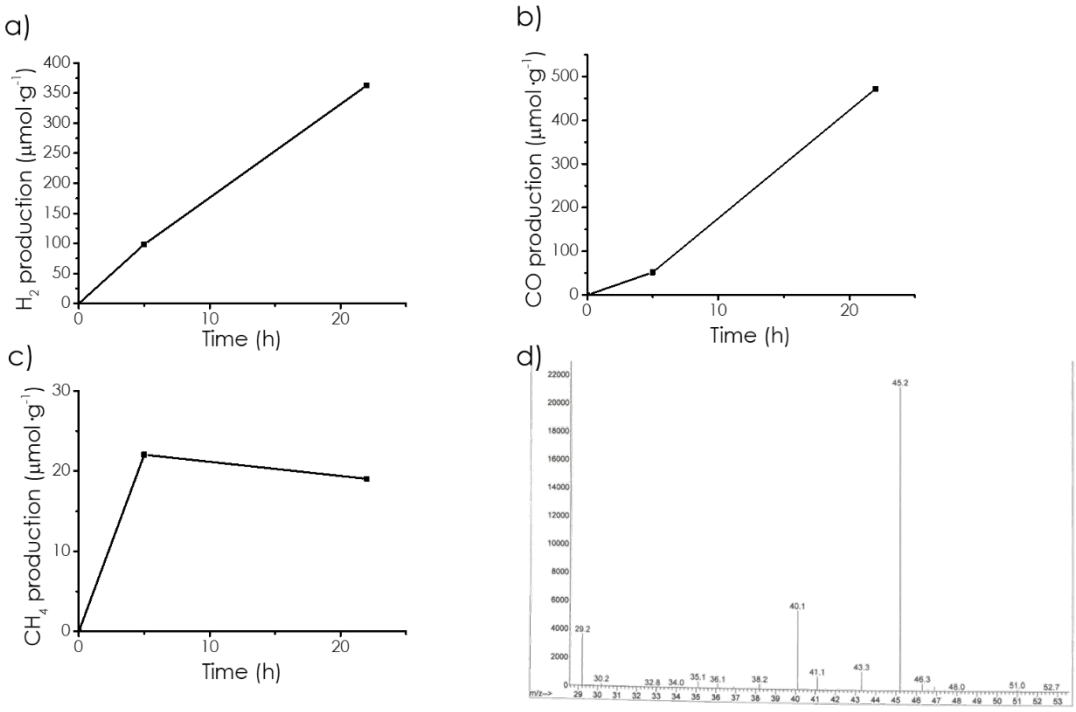

Figure 3. Comparative of the temporal evolution of gases production a) H_2; b) CO c) CH_4 by the different tested materials and d) Mass spectra of the test using ^{13}C.

To determine the origin of CO and CH_4, blank controls under the same conditions replacing CO_2 by Ar were performed, whereby the formation of CO or CH_4 was not observed, except in the case of mp-(N)Cα and mp-(P)Cα or which the presence of CO in minute amounts was observed. Further confirmation of CO_2 as the source of CO and CH_4 in the photocatalytic reactions was obtained by using ^{13}C-labelled CO_2 in the reaction with mp-Cα photocatalyst and analyzing the products by mass spectrometry. This technique reveals the presence of a peak at m/z 29 amu and the absence of a peak at m/z 28 amu (inset of Fig. 3), providing a firm evidence that all CO derives from $^{13}CO_2$.

The photocatalytic activity of mp-C to promote artificial photosynthesis, promoting CO_2 reduction by H_2O was finally also explored. In these measurements, the experimental conditions are similar except that the triethanolamine volume was replaced by additional H_2O. In these reactions CH_3CN (12 mL) and H_2O (8 mL) were used as solvent mixture using the same mp-C weight (16 mg). In these reactions, the products observed were H_2 (30 $\mu mol \times h^{-1}$), CO (2 $\mu mol \times h^{-1}$) and O_2. Formation of CH_4 could not be detected under these condition. The temporal product evolution is presented in Fig. S8. These results are in line with our previous reports showing that mp-C was able to generate photocatalytically H_2 and O_2 from H_2O.[12] A control experiment, in the absence of CO_2 did not show CO evolution. Now if CO_2 is also present, then, photocatalytic CO_2 reduction also occurs concomitantly with overall water splitting. Again, these results are remarkable and in our knowledge unprecedented, since mp-C is composed almost of pure C and no metals or doping elements are presented.

Photocurrent measurements.

To demonstrate the generation of e^- and h^+ upon illumination and to gain further understanding on the photocatalytic activity of mp-C, photocurrent measurements were carried out by depositing on transparent, conductive FTO electrode a well-dispersed suspension of mp-C. Besides mp-C/FTO as photoelectrode, graphite and Ag/AgCl were used as counter and reference electrode, respectively, in 1 M aqueous $KHCO_3$ as electrolyte. Experimental section provides additional detail of the mp-C/electrode area and active mass, as well as preparation procedure and measurement, while Fig. 4 presents a summary of the photocurrent measurements and supporting information.

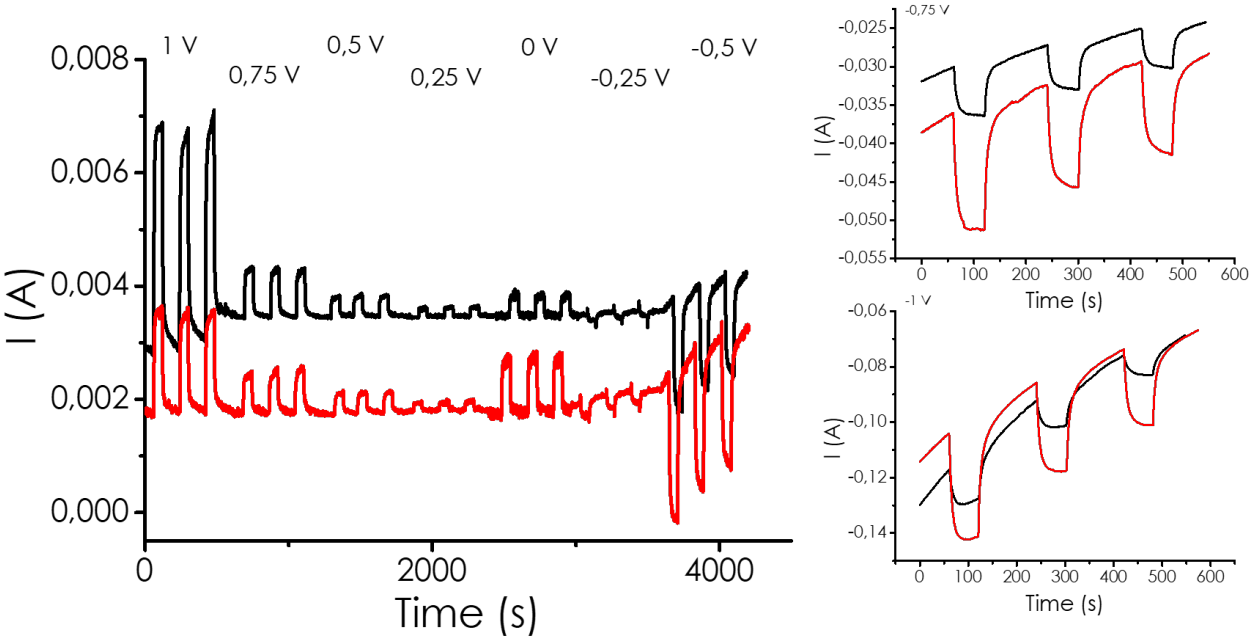

Figure 4. Photocurrent measurements, bubling in the electrolite N_2 in black and CO_2 in red.

Prior characterization of the polarization curves for mp-C/FTO photoelectrodes indicate that they could be used in the range of potential from 1 to -0.5 V vs Ag/AgCl, since at -1 V vs. Ag/AgCl there was a strong discharge due to the hydrogen evolution reaction (HER). Measurements were carried out under N_2 and CO_2-saturated conditions. Large currents were observed at 1 V vs. Ag/AgCl bias potential with no difference on the gas present in the measurement. This indicates that all the charge carriers are mobilized under these extreme conditions. In contrast at more moderate bias potentials of 0.5, 0.25 and 0 V vs. Ag/AgCl, although the absolute of the photocurrents were obviously lower depending on the extraction voltage, much large enhancements by light were observed upon CO_2 saturation of the electrolyte in comparison to N_2. Positive photocurrents were measured at 0 V vs.

Ag/AgCl bias, observing a change from positive to negative photocurrent beyond -0.25 V vs. Ag/AgCl that should be close to the conduction band potential of mp-C. Beyond this crossover polarization potential, the currents were negative and having higher intensity in the presence of CO_2. While photocurrents prove that mp-C undergoes charge separation upon illumination, polarization indicating that it is an *n*-type semiconductor, the somewhat higher negative photocurrents in the presence of CO_2 as compared to N_2 indicate the occurrence of photocatalytic CO_2 reductions, contributing the process.

Transient absorption spectroscopy.

Photoinduced charge separation kinetics and reactivity can be studied by transient absorption spectroscopy (TAS). Upon irradiation with a 355 nm laser pulse of a CH_3CN suspension of mp-C_α, generation of a TA spectra decaying in the microsecond time scale was observed for all the samples. The spectra consisted in all cases in a continuous absorption spanning the whole available monitoring wavelength (300-760 nm), reminiscent to that of the UV-Vis ground state. Fig. 5 shows a representative spectrum recorded 50 μs after the laser pulse. The temporal profile of all the wavelengths were coincident, indicating that they correspond to a single species or if there are several, they decay by annihilation and contribute to the absorption similarly. Fitting of the transient signal to a first order kinetics show low residuals with a lifetime of 60 μs. Identical features, i.e. featureless continuous transient absorption with coincident temporal decays, were similarly recorded for mp-C_β and mp-C_γ with some lower initial signal intensity.

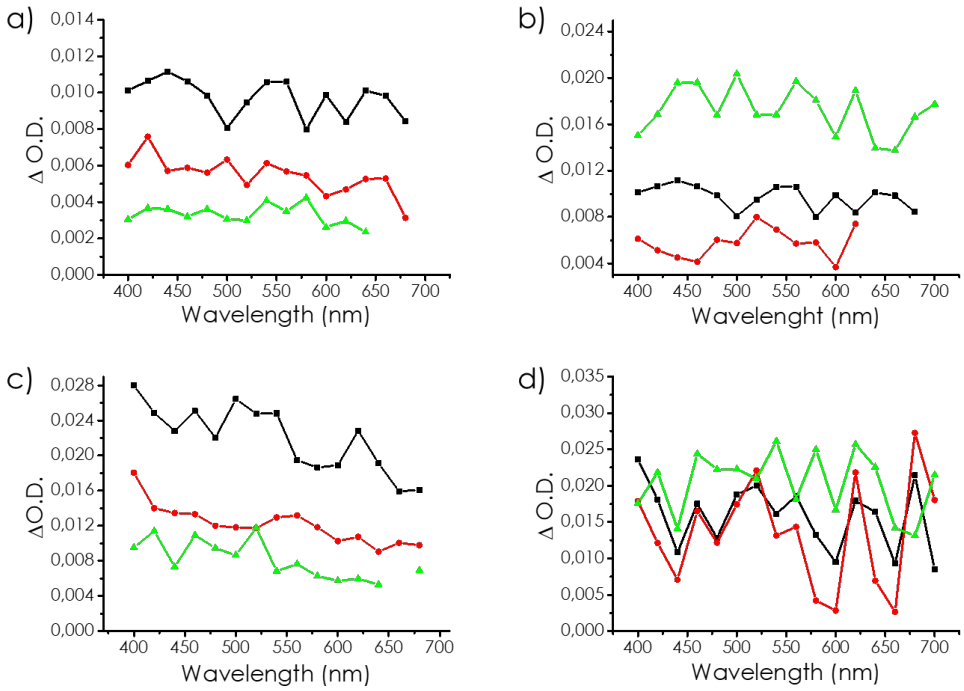

Figure 5. Spectrum recorded at 50 μs of the samples mp-C_α (black), mp-C_β (red) and mp-C_γ (green) in a) N_2 and c) CO_2; and the samples mp-C_α (black), mp(N)-C_α (red) and mp(P)-C_α (green) b) N_2 and d) CO_2.

To gain information of the nature of the signal, particularly if it corresponds to a charge separated state, quenching of the signal by O_2 was studied. In the case of mp-C_α the effect O_2 quenching was marginal with some changes in the intensity and kinetics at 400 and 480 nm and no appreciable changes in the signal at 640 nm. This trend on O_2 quenching was also present, but more remarkable for mp-C_β. We attribute the increase of the signal intensity in the 400-560 nm region to the prevalence of h^+ absorption in this region. In the presence of O_2, some photogenerated electrons will be quenched by O_2, leading to lesser prompt e^-/h^+ recombination and, therefore, to an excess of h^+ that will be reflected in an increase in the intensity of h^+ from 400 to 560 nm. The fact that mp-C_β is more affected than

mp-Cα is due to the difference in pore size. As already commented N_2 is not suitable gas to determine surface area and N_2 and O_2 have similar kinetic diameter.

To further check this proposal, while providing a spectroscopic evidence of the reaction of CO_2 with photogenerated e-, TAS measurements were also performed in the presence of CO_2. Similar behavior was observed for O_2 and CO_2 with a change in the intensity of the temporal profiles and kinetics of the signal in the 480-540 nm region, but no influence at longer wavelengths that should be contributed mostly by unreactive, trapped electrons. In good agreement with our proposal, similar quenching behavior of O_2 and CO_2 was observed as presented in Fig. 6. Notably, the effect of CO_2 was even higher than that of O_2, in spite of being worst electron quencher. We attribute the higher influence of CO_2 to its better ability to diffuse inside the pores of mp-C, as previously commented when describing specific surface area measurements by isothermal CO_2 adsorption in comparison to N_2 adsorption. Therefore, the even higher increase in the intensity of the transient signal at 400 nm is due to the better ability of CO_2 to trap internal electrons in mp-Cα and mp-Cβ.

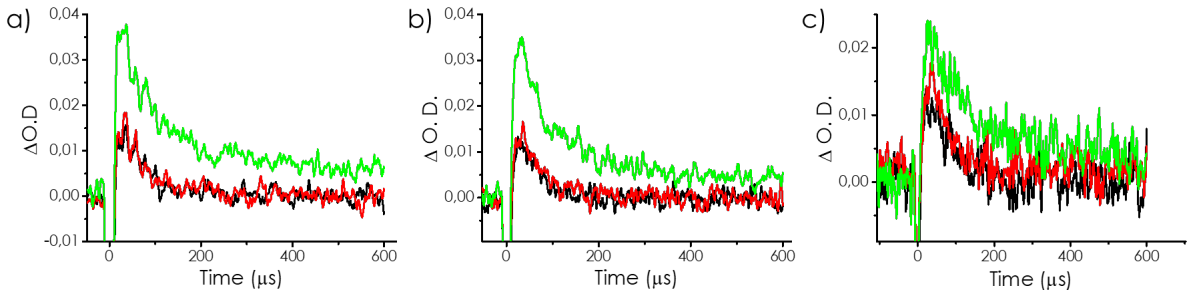

Figure 6. Deactivation kinetics monitored at a) 400 nm, b) 500 nm and c) 600 nm.

Regarding doped mp-(N)C$_\alpha$, surprising its transient signal was very weak, meaning that no much e-/h+ reach the microsecond time scale and that N is promoting charge recombination. It is well-known in semiconductors that an excessive dopant population can promote charge recombination. Apparently, this should be the case of mp-(N)C$_\alpha$.

In contrast, although the signal for mp-(P)C$_\alpha$ were more intense than for mp-C$_\alpha$ and the quenching behavior for O_2 followed the same trend as for mp-C$_\alpha$, no influence of the presence of CO_2 could be monitored. This means that CO_2 is not able to quench photogenerated electrons.

Overall the results of the TAS study explain the photocatalytic activity results, particularly the lack of a positive influence of dopant elements on the photocatalytic activity of mp-C$_\alpha$, but for different reasons. In the case of N-doping due to the short lifetime of the charge separation and in the case of P-doping due to the failure to transfer electrons to CO_2.

Conclusions.

Microporous graphitic carbons derived from cyclodextrin exhibit activity as photocatalysts for CO_2 reduction to CO accompanied by CH_4 in some extent. The process takes place concomitantly with H_2 reduction. The most efficient material in the series was the one having the smallest pore size derived from α-cyclodextrin. This material is constituted by C in over 99 % of its composition and it does not contain any dopant or metal, thus proving the possibility to develop only-carbon photocatalysts. The material exhibits an apparent quantum yield for CO formation of 0.82 % and is stable under irradiation conditions. Photocurrents measurements reveal and enhancement of cathodic

photocurrent in the presence of CO_2, while transient absorption spectroscopy reveal quenching of a fraction of photogenerated e^- by CO_2 in the submicrosecond time scale. No positive influence of N or P doping at the loadings studied was observed. Overall the present results are a rare case of an almost all-carbon photocatalyst being able to reduce photocatalytically CO_2 without the presence of any metal or even doping element.

Acknowledgements.

Financial support by the Spanish Ministry of Science and Innovation (Severo Ochoa and RTI2018-89237-CO2-1) and Generalitat Valenciana (Prometeo 2021/083) are gratefully acknowledged. A.G.-M. thanks the Spanish Ministry of Science and Innovation for a postgraduate scholarship.

Experimental section.

Synthesis of the photocatalyst

0,40 mol of the selected precursor (α-cyclodextrin (>98%, Sigma-Aldrich), β-cyclodextrin (>97%, Sigma-Aldrich) or γ-cyclodextrin (>98%, Sigma-Aldrich)) were dissolved in 20 mL of ultrapure water. For the heteroatom doping, 60 mg of urea or 12 µL of H_3PO_4 were added to the solution too. After 24 h of stirring, it was dried at 60°C in silicone bath. The resulting white powder was pyrolyzed in a horizontal electrical oven by heating at 10 °C × min^{-1} up to 900 °C for 2 h under Ar flux of 200 mL/min. Finally, it was milled for the following tests and characterization.

Physicochemical Characterization

Raman spectra were recorded with 514 nm laser excitation on a Renishaw Raman spectrometer ("Reflex") equipped with a Leica optical microscope and a charged coupled device camera. The laser power in the sample was 25 mW. Each spectrum was the average of 20 acquisitions at a resolution of 4 cm^{-1}.

The XRD pattern was recorded using a Cubix-pro PANalytical diffractometer in the range from 5 to 90° at the scan rate of 1° × s^{-1}.

Diffuse reflectance UV–vis spectra in the range of 200–800 were recorded on a Cary 5000 spectrophotometer from Varian.

Solid-state 31P NMR spectra were measured at room temperature using a Bruker AV400WB with $\pi/2$ pulse sequences of τ = 5 μs and a relaxation time of 5 s. The experiments were carried out with magic-angle spinning at the rate of 10 kHz. For obtaining the spectra, scans between 100 and 400 were accumulated.

The combustion elemental analyses were measured with a Euro EA 3000 analyzer.

TEM images were recorded on a JEOL JEM 2100F with a voltage of 200 kV coupled with an X-Max energy-dispersive X-ray detector (EDS). And FESEM images on a ZEISS ULTRA 55. Samples were prepared by casting one drop of the suspended material in ACN onto a carbon-coated copper TEM grid and allowing it to dry at room temperature.

Photocatalytic tests

The photocatalytic reactions were developed in a 51 mL quartz reactor fitted with a manometer, an inlet valve, and an outlet valve. The irradiation source was a 300 W Xe lamp (Hamamatsu, 1.6 sun power) with a UV−vis light range or a solar simulator (OrielTM, 1 sun power).

The mp-C was dispersed in 30 mL of acetonitrile (>99.9%, Sigma-Aldrich) (ACN) using a Sonic tip (FisherbrandTM Model 705 at 40% of 700 W for 1 h using a pulsation of 1 s on and 1 s off) in a concentration of 1.5 mg × mL^{-1}). 10 mL of this suspension were introduced in the reactor with 4 mL of triethanolamine (Sigma-Aldrich) as electro donor and 4 mL of MilliQ water. To reach the 20 mL of mixture reaction, 2 mL more of ACN were added. The system was purged using pure CO_2 for 10 min and pressurized until 1.4 bar (absolute pressure)

The gas products were analyzed using a gas chromatograph (Agilent 490 MicroGC) equipped with a molecular sieve 5 Å column with a TC detector and Ar as the carrier gas. And for CO, a gas chromatograph 7890A equipped with a column Carboxen®-1010 PLOT L × I.D. 30 m × 0.53 mm, average thickness 30 µm with TC detector and He as carrier gas.

For the stability tests, the material was removed from the reactor between the reactions and washed 3 times by centrifugation (6000 rpm, 15 min) using MilliQ water before starting a new reaction.

Value of apparent quantum yield (AQY) were determined under irradiation with a 150 W Xe lamp equipped with a Czerny Turner monochromator. The AQY value was calculated using:

$$AQY = \frac{Number\ of\ evolved\ CO\ molecules\ x\ 2}{Number\ of\ inciednt\ photons}$$

Photoelectrochemical measurements.

Photoelectrochemical measurements were developed in a 3-electrode electrochemical cell using Ag/AgCl as reference electrode, graphite as counter electrode and the mp-C_α deposited on

florine-doped tin oxide (FTO) as working electrode. A solution 0.5 M of $KHCO_3$ was used as electrolyte.

During the measurements, N_2 or CO_2 were bubbled in the solution to have the electrolyte completely saturated. And each measurement was done twice in two different electrodes to confirm the material behavior.

Notice that the photocatalyst was deposited on the FTO using a mixture of 15 mg of ultrasonicated photocatalyst (the ultrasonication was developed in 15 mL of ethanol 40%, 1 h, 1 son, 1 s off and dried at 60°C) in 300 µL of ethanol and 75 µL of Nafion 5% (w:w). The electrode was dried at room temperature overnight. The characteristic of each electrode are in the following table:

Table 2. Characteristic of the electrodes.

Electrode	Surface area (cm^2)	Active mass (mg)
E1	0.7	3.4
E2	0.65	5.3

For the chromoamperometric tests, the electrode was let to get stabilized for 5 min at the selected potential (1 V, 0.75 V, 0.5 V, 0.25 V, 0 V, -0.25 V, -0.5 V, -0.75 V or -1 V vs the reference electrode). After that, the electrode was irradiated for 1 min using the same Xe lamp that was used in the photocatalytic tests and it was let relaxing for 2 min. This was repeated 5 times for each potential to confirm the reproducibility of the tests.

For the cyclovoltametry tests, the scan speed was 0.02 $V \times s^{-1}$, from 1 V to -1 V vs the reference electrode, 5 cycles.

Transient absorption measurements

Transient absorption spectra were recorded using the forth harmonic of a Q switched Nd:YAG laser (Quantel Brilliant, 266 nm, 15 mJ/pulse, 7 ns fwhm) coupled to a mLFP122 Luzchem miniaturized detection equipment. The studied suspension had a concentration of 0.5 mg × mL^{-1} of the mc-C_α in ACN. This transient absorption spectrometer includes a 300 W ceramic xenon lamp, 125 mm monochromator, Tektronix TDS-2001C digitizer, compact photomultiplier and power supply, cell holder and fibre-optic connectors, computer interfaces, and a software package developed in the LabVIEW environment from National Instruments. The laser flash generates a 5 V trigger pulses with programmable frequency and delay. The rise time of the detector/digitizer is ~3 ns up to 300 MHz (2.5 GHz sampling). The monitoring beam is provided by a ceramic xenon lamp and delivered through a fibre-optic cable. The laser pulse is probed by a fibre that synchronizes the photomultiplier detection system with the digitizer operating in the pretrigger mode.

References.

(1) Tran, P. D.; Wong, L. H.; Barber, J.; Loo, J. S. Recent advances in hybrid photocatalysts for solar fuel production. *Energy & Environmental Science* **2012**, *5*, 5902-5918.

(2) Fujishima, A.; Honda, K. Electrochemical photolysis of water at a semiconductor electrode. *nature* **1972**, *238*, 37-38.

(3) Hashimoto, K.; Irie, H.; Fujishima, A. TiO2 photocatalysis: a historical overview and future prospects. *Japanese journal of applied physics* **2005**, *44*, 8269.

(4) Bard, A. J. Photoelectrochemistry and heterogeneous photo-catalysis at semiconductors. *Journal of Photochemistry* **1979**, *10*, 59-75.

(5) Su, D. S.; Zhang, J.; Frank, B.; Thomas, A.; Wang, X.; Paraknowitsch, J.; Schlögl, R. Metal-free heterogeneous catalysis for sustainable chemistry. *ChemSusChem: Chemistry & Sustainability Energy & Materials* **2010**, *3*, 169-180.

(6) Navalon, S.; Dhakshinamoorthy, A.; Alvaro, M.; Garcia, H. Carbocatalysis by graphene-based materials. *Chemical reviews* **2014**, *114*, 6179-6212.

(7) Navalon, S.; Dhakshinamoorthy, A.; Alvaro, M.; Antonietti, M.; García, H. Active sites on graphene-based materials as metal-free catalysts. *Chemical Society Reviews* **2017**, *46*, 4501-4529.

(8) Li, C.; Xu, Y.; Tu, W.; Chen, G.; Xu, R. Metal-free photocatalysts for various applications in energy conversion and environmental purification. *Green Chemistry* **2017**, *19*, 882-899.

(9) Albero, J.; Peng, Y.; García, H. Photocatalytic CO2 reduction to C2+ products. *ACS Catalysis* **2020**, *10*, 5734-5749.

(10) Shen, H.; Peppel, T.; Strunk, J.; Sun, Z. Photocatalytic reduction of CO2 by metal-free-based materials: recent advances and future perspective. *Solar RRL* **2020**, *4*, 1900546.

(11) Albero, J.; Mateo, D.; García, H. Graphene-based materials as efficient photocatalysts for water splitting. *Molecules* **2019**, *24*, 906.

(12) Peng, Y.; Rendón-Patiño, A.; Franconetti, A.; Albero, J.; Primo, A.; Garcia, H. Photocatalytic Overall Water Splitting Activity of Templateless Structured Graphitic Nanoparticles Obtained from Cyclodextrins. *ACS Applied Energy Materials* **2020**, *3*, 6623-6632.

(13) Rendón-Patiño, A.; Santiago-Portillo, A.; Vallés-Garcia, C.; Palomino, M.; Navalón, S.; Franconetti, A.; Primo, A.; Garcia, H. Templateless Synthesis of Ultra-Microporous 3D Graphitic Carbon from Cyclodextrins and Their Use as Selective Catalyst for Oxygen Activation. *Small Methods* **2020**, *4*, 1900721.